



ORIGINAL RESEARCH ARTICLE

Study on Dry Sliding Friction and Wear Properties of Detonation Spray Fe-Based Amorphous Coatings

Chunling Li, Rongfu Wang, Xingyu Xu, Shaobing Li, Haimin Zhai, and Wensheng Li

Submitted: 27 August 2023 / Revised: 24 October 2023 / Accepted: 26 November 2023

Fe-based amorphous coatings (AMCs) were applied onto 316L stainless steel using the detonation spraying technique. Friction and wear experiments were conducted under varying normal loads (5N and 10N) and sliding speeds (0.1-0.3 m/s) to investigate the microstructure, as well as the dry sliding friction and wear behavior of the coating. The findings reveal that the Fe-based AMC exhibits a fully amorphous structure, with measured thickness, porosity, and surface hardness values of $174 \pm 10 \mu\text{m}$, 1.2 vol.% and $783 \pm 8 \text{HV}_{0.1}$, respectively. When subjected to dry sliding wear conditions, the coating demonstrates favorable wear resistance, with a wear rate ranging from $(0.16\text{-}2.53) \times 10^{-6} \text{mm}^3 \text{N}^{-1} \text{m}^{-1}$. As the normal load and sliding velocity increase, the wear mechanism of the coating gradually transitions from oxidation wear to delamination wear, with minimal abrasive wear observed. Furthermore, the results indicate that the impact of the applied normal load on the wear rate of Fe-based AMCs is more pronounced than that of the sliding speed, particularly at higher sliding speeds.

Keywords 316L stainless steel, detonation spraying, dry sliding wear, Fe-based amorphous coating, wear mechanism

1. Introduction

In the machinery manufacturing industry, 316L stainless steel is extensively utilized due to its favorable mechanical properties and outstanding corrosion resistance. It finds widespread application in various fields such as aerospace, chemical industry, nuclear industry, and ocean engineering (Ref 1-4). However, the widespread use of 316L stainless steel is greatly hindered by its low hardness and wear resistance (Ref 3). Some scholars have found that boron-doped on the surface of a steel substrate can change its crystalline phase structure, increase the hardness of the substrate, reduce the friction coefficient, and decrease the wear rate of the coating (Ref 5-7). Recently, Fe-based amorphous alloys have drawn a lot of interest because of their strength, high hardness, strong mechanical properties, wear and corrosion resistance, as well as their affordability (Ref 8-10). Despite these extraordinary qualities, their applicability as structural materials is nevertheless constrained by their low fracture toughness and limited capacity to produce glass (Ref 11). By applying Fe-based amorphous alloys as a protective surface coating on 316L stainless steel substrate, the limitations of bulk amorphous alloy materials can be overcome (room temperature brittleness, limited critical size) while maintaining their outstanding wear and corrosion resistance (Ref 12-14).

This has significant practical value in industrial settings and holds great potential for further development.

The fabrication of Fe-based ACs has made considerable use of thermal spraying techniques such as high-velocity oxygen fuel (HVOF) spraying (Ref 15, 16), high-velocity air fuel (HVOF) spraying (Ref 17, 18), air plasma spraying (APS) (Ref 19, 20), and detonation spraying (Ref 21, 22). The effects of various spraying methods and process variables on the microstructure, hardness, porosity, and corrosion resistance of Fe-based AMCs have been the subject of numerous investigations. Under diverse circumstances, the wear processes of Fe-based AMCs have also been researched. The sliding velocity, powder size, microhardness, porosity, and amorphous content are some of the variables that affect the coatings' wear resistance and wear mechanisms. Koga et al. (Ref 23) studied the dry sliding friction and wear behavior of Fe-based AMC coated with HVOF and revealed that oxidation wear mostly accounts for the wear mechanism and that the sliding velocity has minimal bearing on the wear of the coating. The high amorphous phase concentration, high hardness, low oxygen content (0.41%), and comparatively low porosity are responsible for the material's exceptional wear resistance. Mahade et al. (Ref 24) studied the wear resistance of HVOF and HVAF-sprayed Fe-based AMCs and discovered that the coating's wear resistance is correlated with its microhardness, porosity, and amorphous content and that the wear rate increases obviously as the normal load increases. Adhesive wear, abrasive wear, and oxidation wear are the wear mechanisms. The research of Zhang et al. (Ref 25) shows that the main wear mechanism of coatings is fatigue wear accompanied by oxidation wear. Powder size has a considerable impact on the wear resistance of APS-sprayed Fe-based AMCs. Obviously, the preparation process and a few variables, such as coating density, amorphous phase content, and microhardness, might affect how Fe-based AMCs wear. Among these methods, detonation spraying offers advantages such as low porosity and high amorphous content in the resulting coatings. As a result, analyzing the microstructure

Chunling Li, Rongfu Wang, Xingyu Xu, Shaobing Li, Haimin Zhai, and Wensheng Li, School of Mechanical and Electrical Engineering, Lanzhou University of Technology, Lanzhou, China. Contact e-mails: yxplcl@lut.edu.cn and LIws@lut.edu.cn.

changes and studying the wear mechanism of Fe-based AMCs prepared by detonation spraying can provide valuable insights.

In this study, the detonation spraying-prepared Fe-based AMC was put to the test for wear behavior under different sliding speeds and normal loads. The microstructure and surface microhardness of the coating were analyzed before and after the wear test to understand the wear resistance and wear mechanisms of the Fe-based AMCs under various wear conditions. Ultimately, the findings from this research contribute to the understanding and application of Fe-based AMCs in industrial settings, highlighting their potential for improving wear resistance and extending the service life of workpieces.

2. Experimental Content

An Fe-based AMC was applied on a 316L stainless steel substrate ($100 \times 100 \times 8$ mm) using detonation spraying equipment (AEM-DGUN). Prior to spraying, a mixture of acetone and ethanol was used to clean the stainless steel substrate's surface and get rid of any remaining oil. The substrate was then alumina abrasively sandblasted to improve the adherence between the coating and substrate. Table 1 provides an overview of the main groups of commercial Fe-based amorphous powders used in the study. The technical parameters related to the detonation spraying process are listed in Table 2. X-ray diffraction (XRD, Bruker D8) was used to analyze the phases of the Fe-based amorphous powders and coatings at a scanning rate of $0.02^\circ/\text{s}$, a diffraction Angle of 2θ , and a scanning range from 20° to 90° . Using a laser particle size analyzer (Mastersizer 2000), the size of the powder particles in the Fe-based amorphous materials was determined. Additionally, the fluidity of the powders was assessed with a Hall flowmeter. The microstructure of the Fe-based AMCs was observed using a scanning electron microscope (SEM, Tescan Mira4). Using a Vickers microhardness tester (HV-1000), the coating's cross sectional microhardness was determined. A load of 100 g was applied with an indentation time of 10 s. Ten measurements were taken to obtain the average hardness. Software called Image-Pro Plus 6 was used to calculate the porosity of the Fe-based AMC. To determine the average percentage of porosity, at least 15 SEM pictures with a $200\times$

Table 1 Fe-based amorphous powder mass fraction table

Element	Cr	Mo	C	B	Fe
Wt. %	25-27	16-18	2.0-2.5	2.0-2.2	Bal.

Table 2 Process parameters of detonation spraying

Parameters	values
Working gas	$\text{O}_2 + \text{H}_2\text{C}_2 + \text{N}_2$
Oxygen-fuel ratio/ m^3h^{-1}	0.5
Nitrogen flow/ m^3h^{-1}	0.05
Working frequency/Hz	4.0
Spraying distance/mm	140

magnification were chosen at random from the polished surface.

The unidirectional ball and disc wear testing machine (HT-1000) was utilized to conduct the experiments. The friction pair was chosen to have a Si_3N_4 ball with a diameter of 6 mm and a hardness of 1650 ± 80 Hv. Fe-based AMCs were subjected to dry sliding friction and wear tests at different loads (5N, 10N) and sliding velocities (0.1-0.3 m/s). For 30 min, the wear track's diameter was set at 6 mm. The coated samples were polished to obtain a surface roughness of under 500 nm before carrying out the friction and wear tests. Following the friction and wear experiments, the three-dimensional contour of the wear marks was observed using a white light interferometer, and the wear marks were measured using a probe measuring machine (MT500). At least three contour measuring traces were obtained from each wear surface to calculate the wear volume. Using the equation $W_r = V_w F_N / L$, it was possible to calculate the wear rate (W_r) of the coating under various wear situations, where F_N and L stand for the applied load (N) and sliding distance (m), respectively, and V_w stands for the wear volume (mm^3). Additionally, using SEM and an energy dispersive spectrometer (EDS, Xplore30. Aztec one), the wear marks, related cross sections, and chips were examined and classified. Moreover, X-ray photoelectron spectroscopy (XPS, Thermo SCIENTIFIC ESCALAB Xi+) was used to do a qualitative and semi-quantitative characterization of the surface components of the Fe-based AMC wear scars. The acquired spectra were fitted using Avantage software.

3. Results and Discussion

3.1 Characterization of Fe-Based Amorphous Powders and Coatings

Figure 1(a) illustrates the SEM image of the Fe-based amorphous raw material powder used in the detonation spraying process to prepare the coating. The image shows that most of the powder particles are spherical in shape and have smooth surfaces. The powder's fluidity, as measured by the Hall flowmeter (3.828 s/50 g), demonstrates excellent flow properties, indicating its suitability for the detonation spraying process. The size distribution of the Fe-based amorphous powder is shown in Fig. 1(b), with particle sizes mostly ranging between 10 and 40 μm , which meets the criteria of the detonation spraying method. Moving on to Fig. 2(a), the XRD patterns of the gas-atomized Fe-based amorphous powders are presented. Notably, These powders show a prominent broad hump peak in the 2θ angle range of 30° to 55° with no obvious crystalline peaks, confirming the Fe-based amorphous powder and the resultant coating's amorphous structure similarities. Figure 2(b) demonstrates that the element distribution on the surface of the sprayed coating is consistent with that of the powder. The amorphous structure of the Fe-based AMC is well maintained by this successful detonation spraying method.

Figure 3(a) displays the unpolished surface of the Fe-based AMC. Unmelted and partially-melted particles can both be found on the coating's surface. The occurrence is caused by some particles not receiving enough heat during the spraying process, which only partially melts the surface. However, the coating surface spreads uniformly as a whole. Figure 3(b) illustrates the polished Fe-based AMC's cross sectional mor-

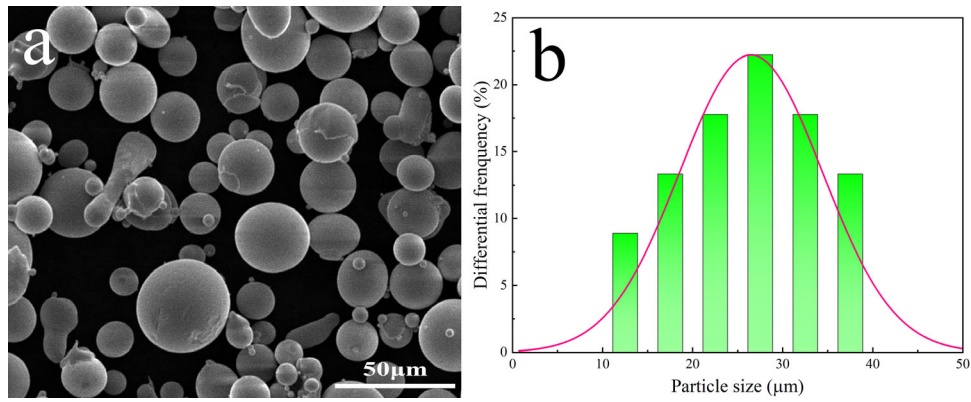


Fig. 1 SEM image of (a) atomized Fe-based amorphous powder (b) raw material powder particle size dispersion

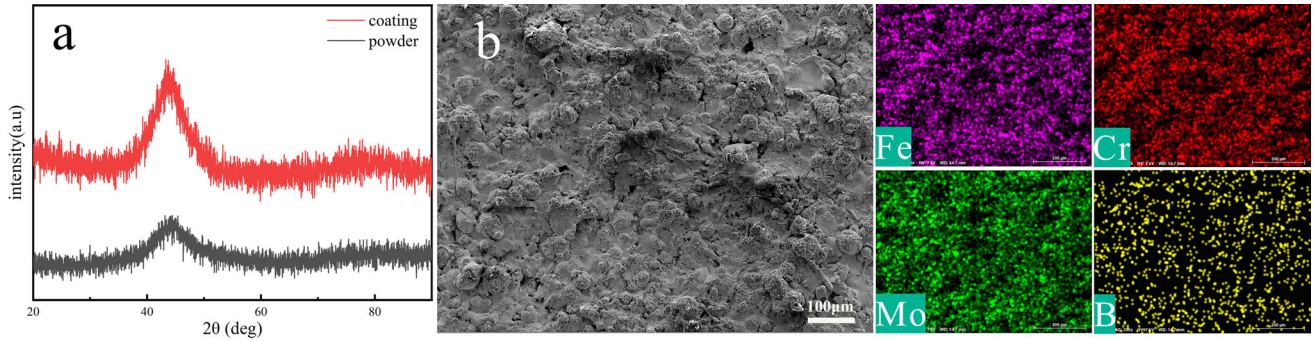


Fig. 2 X-ray diffraction pattern of (a) Fe-based amorphous raw material powder and coating (b) surface element distribution of coating

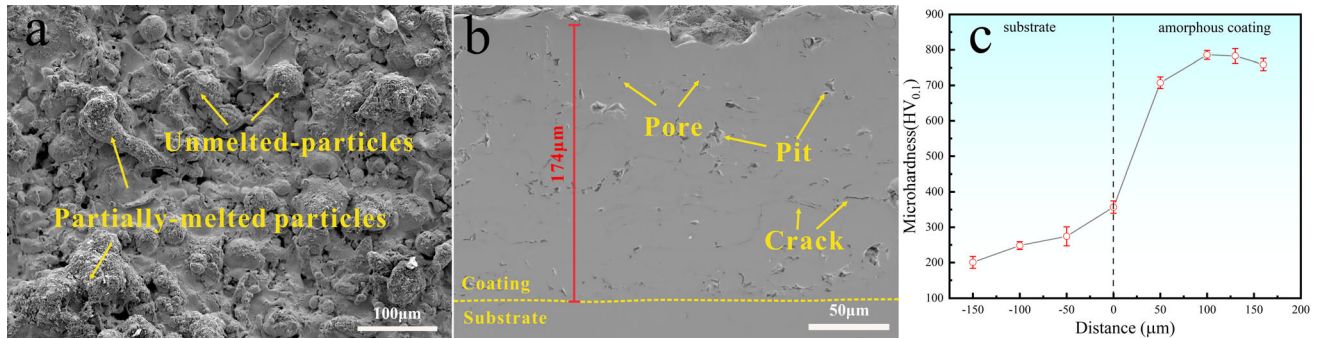


Fig. 3 Surface morphology (a) cross section morphology (b) and hardness distribution (c) on the cross section surface of Fe-based AMCs

phology. It is obvious that the coating is tightly attached to the 316L stainless steel substrate and has a thickness of $174 \pm 10 \mu\text{m}$. The porosity of the coating, measured using image-Pro Plus 6 image analysis software, is found to be 1.2 vol.%. The density of the coating primarily stems from the supersonic flight speed (1200 m/s) of the powder particles during the detonation spraying process (Ref 26). The 316L substrate experiences strong mechanical bonding forces because of the powder particles' high-speed impact, creating a thick and well-bonded coating structure. The Vickers hardness distribution curve of the Fe-based AMC's cross section is shown in Fig. 3(c). It can be observed that the Vickers hardness gradually increases from the substrate toward the coating. There is a slight increase in hardness at the joint of the coating and the substrate. This effect is explained by deformation strengthening caused by the powder particles' significant impact on the

substrate. The coating has a much higher Vickers hardness than the 316L stainless steel substrate. The coating's average Vickers hardness ($761 \pm 10 \text{Hv}$) is around 3.3 times greater than the 316L stainless steel substrate's ($214 \pm 3 \text{Hv}$). The higher hardness of the Fe-based AMC considerably increases its wear resistance, as shown by the Archard equation (Ref 27).

3.2 Tribological Properties of Fe-Based ACs

Figure 4 illustrates the coefficient of friction (COF) curve obtained from dry sliding friction and wear experiments conducted on the Fe-based AMC and 316L substrate, using a Si_3N_4 ball as the friction pair. In Fig. 4, after a brief run-in period, all COF curves arrive at a stable period. This is explained by the fact that despite polishing ($R_a = 0.045 \mu\text{m}$), the coated surface still has some degree of roughness. As a result, when the unevenly coated surface makes contact with

the counterpart, an unstable resistance results, causing large changes in COF. The noticeable surface imperfections on the coating gradually diminish as the test goes along, resulting in a stable COF (Ref 17). The COF run-together residence time is shorter (2 min) for the Fe-based AMC with a sliding velocity of 0.1 m/s than it is for the 316L substrate (5 min). This indicates that the Fe-based AMC demonstrates good friction stability. Two factors (Ref 28, 29): local fracturing of the worn surface and the production and spalling of new wear chips, are responsible for the sharp and significant changes in the coating's coefficient of friction (COF) at the sliding velocity of 0.3 m/s. The average COF value of the coating increases with sliding velocity, rising from 0.786 at 0.1 m/s to 0.862 at 0.3 m/s. This rise may be related to a switch from oxidation wear to delamination wear under cyclic load in the wear process. In Fig. 4(b), the average COF of the coating exhibits a downward trend with increasing sliding speed under load of 10N, in contrast to the overall decrease in COF under load of 5N. This is explained by the rise in heat produced during frictional motion under heavier loads. Under the influence of high-load cyclic stress, the wear chips produced on the coating

surface undergo a certain degree of oxidation, resulting in a self-lubricating effect and a decrease in COF (Ref 30).

Figure 5 presents the three-dimensional (3D) profiles of the worn on the Fe-based AMC and the 316L substrate. At 0.1 m/s, the wear width and volume of the Fe-based AMC are lower than those of the substrate, demonstrating higher wear resistance under the same sliding conditions. The wear width and volume of the coating increase according to the sliding speed. It can be seen from this, together with the two-dimensional contour curves in Fig. 6(a) and (b), that the depth and width of wear markings rise in direct proportion to the applied load and sliding velocity. Notably, at 0.2 m/s (Fig. 6b), the depth ($5.97 \rightarrow 13.33 \mu\text{m}$), width ($583 \rightarrow 824 \mu\text{m}$), and wear area ($460 \rightarrow 2483 \mu\text{m}^2$) of the wear mark experience significant increases, with the wear area expanding by approximately five times. The wear rate of the 316L substrate and the Fe-based AMC are illustrated in Fig. 6(c) with different normal loads moving at a sliding speed of 0.1 m/s. The wear rate of the Fe-based AMC is more than twice as low as that of the substrate at a load of 5N. The substrate wears down at a rate that is around five times higher than the Fe-based AMC does under 10N.

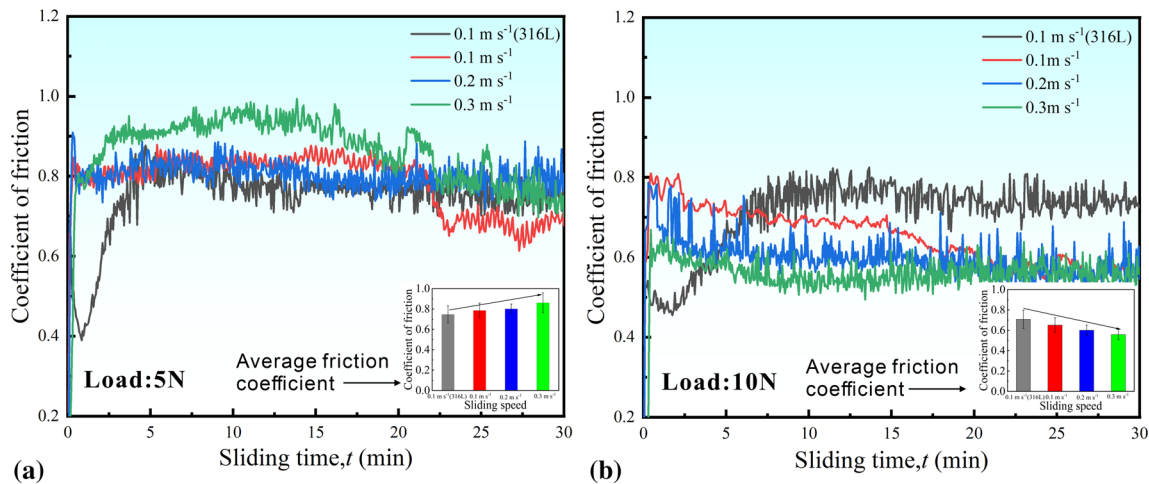


Fig. 4 Curves of friction coefficient at normal load (a) 5N (b) 10N

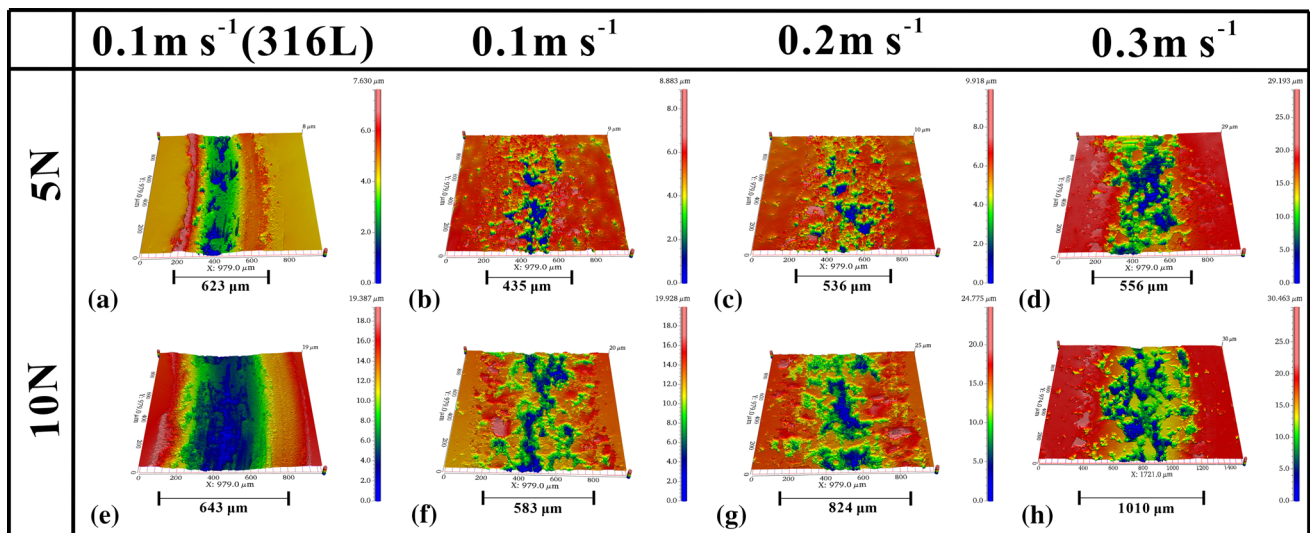


Fig. 5 3D profiles of Fe-based AMC and 316L substrate under different loads and sliding speeds

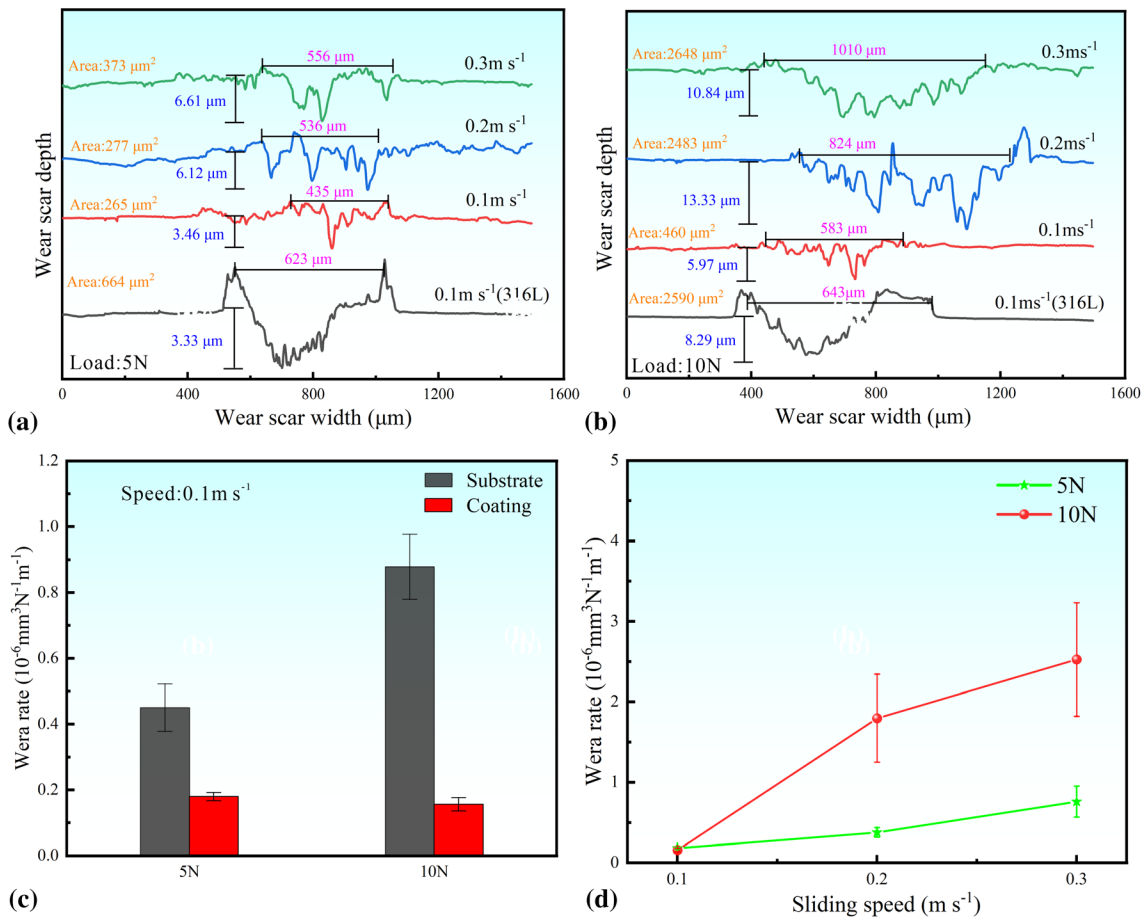


Fig. 6 Frictional wear results of dry sliding wear test: (a) (b) two-dimensional profiles curves of Fe-based AMCs and substrates at different sliding speeds under normal loads of 5N and 10N, respectively (c) Wear rate of Fe-based AMC and substrate under different normal loads at 0.1m/s (d) The wear rate of Fe-based AMCs varies with sliding speed under different normal loads

Comparing the Fe-based AMC produced by detonation spraying to the 316L substrate, this shows a considerable improvement in wear resistance. The wear rate of the Fe-based AMC steadily rises with increasing load and sliding speed, as seen in Fig. 6(d). At 5N, the wear rate increases from 0.18×10^{-6} to $0.76 \times 10^{-6} \text{mm}^3 \text{N}^{-1} \text{m}^{-1}$. At 10N, the wear rate increases from 0.16×10^{-6} to $2.53 \times 10^{-6} \text{mm}^3 \text{N}^{-1} \text{m}^{-1}$. At 10N, the wear rate rises from 0.16×10^{-6} to $1.8 \times 10^{-6} \text{mm}^3 \text{N}^{-1} \text{m}^{-1}$ as the sliding velocity increases (0.1 m/s to 0.2 m/s). A rapid shift in the wear mechanism may be responsible for the significant increase in the Fe-based AMC's wear rate; this is thoroughly discussed in the 3.3 and 3.4 sections.

3.3 Wear Morphology Analysis of Fe-Based AMCs

Figure 7 illustrates the wear surface of the Fe-based AMC under different normal loads and sliding speeds. Figure 7(a), (b) and (c) show that a significant number of white adhesive layers are spread out across the wear surface over the prescribed load and sliding speed range. In Fig. 7(a) and (b), the worn surface of the Fe-based AMC and the accompanying fragments are shown with magnified SEM morphology at 0.3 m/s and 5N, respectively. The worn surface displays evident white adhesive layers and cracks (Fig. 8a); while, the corresponding morphology of the wear chips exhibits a granular structure (Fig. 8b).

Figure 8(c) illustrates the results of the EDS examination of the worn surface (areas 1, 2, and 3 in Fig. 8a) and the wear chips (points 1 and 2 in Fig. 8b). The EDS analysis confirms that the wear chips closely resemble the components of the wear surface, indicating material transfer resulting from cyclic contact stress during dry sliding wear of Fe-based AMCs. The EDS investigation further demonstrates that the wear surface and wear chips both contain more than 55 at.% oxygen, indicating severe oxidation of the Fe-based AMC. Thus, an oxide layer can be recognized as the bonding layer. Additionally, a few grinding pits are evident on the worn surface, accompanied by flaky grinding chips with a maximum size of $14.9 \mu\text{m}$ (Fig. 8b). It can be assumed that the chip peels off from the Fe-based AMC because of cyclic contact stress because the chip and the worn surface have comparable chemical compositions. Moreover, different grinding chips exhibit varying surface oxygen content (point 1 versus point 2 in Fig. 8b), indicating the occurrence of new coating processes. This suggests layered wear after the breakage of the oxide layer under cyclic stress. As a result, oxidation wear and a minor degree of delamination wear make up the coating's wear mechanism.

Figure 7(d), (e) and (f) depicts the wear morphology image under a normal load of 10N and sliding speeds ranging from 0.1 to 0.3 m/s. The worn surface exhibits large grinding pits,

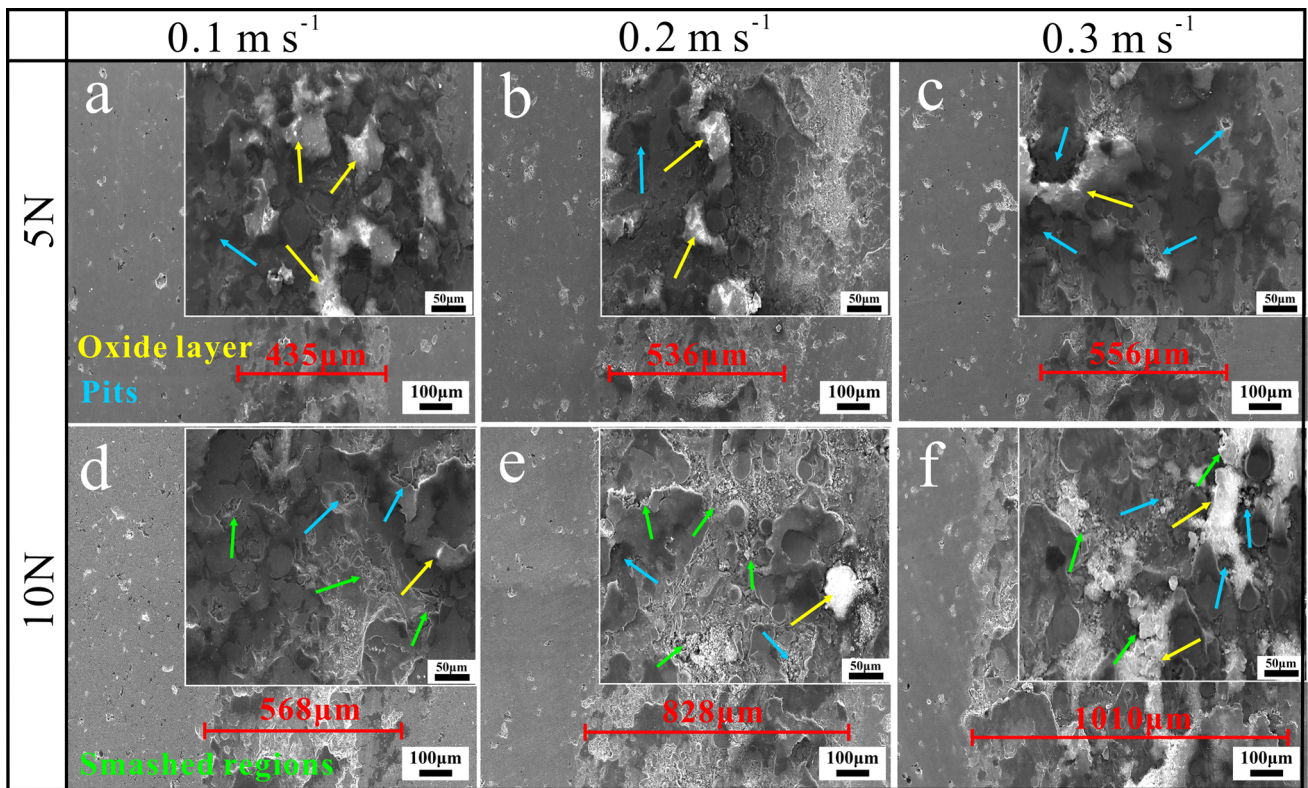


Fig. 7 SEM images of wear surface morphologies of Fe-based AMCs under different normal loads (5 and 10N) and sliding velocities (0.1-0.3 m/s)

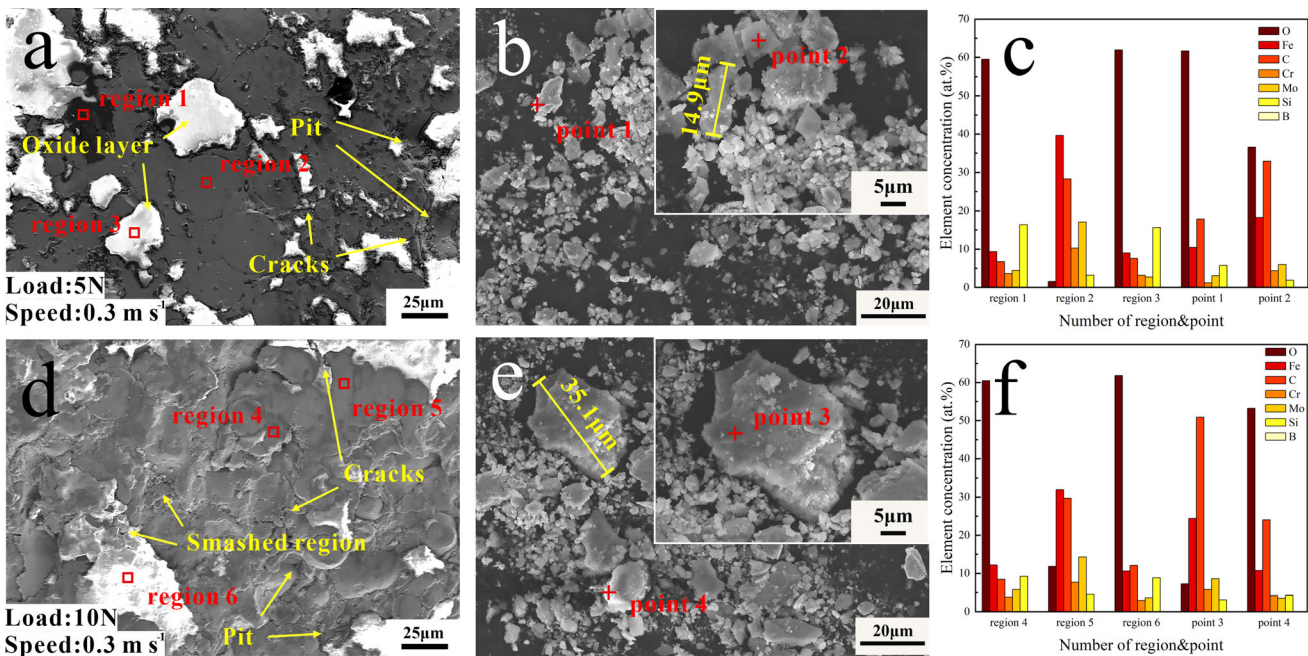


Fig. 8 SEM morphology and EDS results of the corresponding debris on the worn surface and coating: (a) (b) (c) sliding velocity at 0.3 m/s and the normal load of 5N; (d) (e) (f) The sliding speed is 0.3m/s and the normal load is 10N

smooth areas, and gray flaky protrusions. Similar to the tendency seen under 5N, when the velocity of sliding increases, the area of the smooth surface declines noticeably; while, the area of worn pits and gray protrusions increases. This suggests that with increasing sliding velocities and normal loads, the

proportion of multilayer wear in the Fe-based AMC steadily rises. The breadth of the wear markings changes much less when the sliding speed rises, under the same normal load, it is crucial to observe. Taking these findings as a whole, it can be shown that an increase in normal load greatly widens and

deepens the wear traces (Fig. 6a and b), suggesting greater wear of the coating. Additionally, the wear morphology of the Fe-based AMC at 0.2 m/s (Fig. 7e) differs significantly from that at 0.1 m/s (Fig. 7d). At 0.1 m/s, the wear surface mostly consists of a few pits and a white oxide coating, whereas at 0.2 m/s, the wear surface consists of many pits, cracks, warping, and broken areas. Similarly, at 5N and 0.2 m/s (Fig. 7b), both the grinding pits and the areas of adhesion increase significantly, suggesting the delamination wear becoming dominant. Increases in the quantity of grinding pits and the degree of crushing on the coated surface are seen when the sliding speed is raised to 0.3 m/s. Additionally, a few white granular grinding chips are found inside the grinding pits; while, most of the other grinding chips exhibit flaking, with a maximum size of 35.1 μm (Fig. 7f and 8e). The matching EDS data are displayed in Fig. 8(f) and are comparable to those in Fig. 8(c) in that they clearly reveal a high oxygen concentration in the shattered region (region 6), as well as granular debris (point 4). Notably, compared to Fig. 8(c), the oxygen content on the grinding chips in Fig. 8(f) is slightly reduced. This is due to the coating quickly forming fresh spalling once the oxidation layer peels off when exposed to high cyclic contact stress.

The wear rate of Fe-based AMC under different dry friction and wear sliding speeds can be attributed to the cyclic stress and oxidation behavior of the coating surface. At 5N and 0.1 m/s, the wear surface will produce an oxide layer due to the increase in the coating surface temperature caused by friction (as depicted in Fig. 7a). It can be seen from the SEM image that there is a massive oxide layer on the surface of the coating, and a few cracks can be seen from the cross section. When the cracks on the surface of the oxide layer reach a critical size, the applied shear force leads to the destruction of the oxide layer, resulting in variations in the COF. On the other hand, at 10N and 0.1 m/s, obvious delamination and spalling pits are observed on the coating surface (as shown in Fig. 7d); while, the oxygen content on the surface of the coating decreases. This can be attributed to the rapid cracking of the oxide layer on the coating surface under the influence of high shear force. The cracks expand and connect with adjacent cracks under cyclic stress. When the cracks reach the surface of the coating, stratification occurs, resulting in coating fracture and spalling (Ref 31).

At 0.2 m/s, the coating surface shows substantial grinding and crushing areas compared to the worn surface at 0.1 m/s, and the coating delamination phenomenon worsens. Inferred from the presence of multiple pits and cracks on the wear marks of Fe-based AMCs is the increased frequency of cyclic stress, which encourages the creation and propagation of micro-cracks between neighboring coatings (as observed in SEM images, Fig. 7b and e). Under 5N, there is still an oxide layer on the coating surface, but some areas crack, break, and flake under shear force, leading to delamination wear (Fig. 9b). Oxidative wear and layered wear coexist on the coating surface in this case. Additionally, under 10N, the wear mark shows no smooth and flat area, and the wear rate of the coating accelerates significantly (Fig. 6d). Additionally, the coating layer peels off in the presence of cracks when subjected to shear strain. On the worn surface, grinding pits and oxide layers can be seen, and the area of the grinding pits increases as the load and sliding speed rise. These results indicate a transitional shift from slight delamination wear accompanied by oxidative wear to severe delamination wear.

Even more severe stripping and delamination wear on the surface of the Fe-based AMC is caused by the higher-frequency

cyclic stress when the sliding speed is increased to 0.3 m/s (Fig. 9c and f). The depth of the grinding pits increases significantly compared to the sliding speeds of 0.1 and 0.2 m/s. Moreover, the presence of numerous grinding pits and broken areas on the wear marks highlight a more pronounced peeling and delamination wear behavior. The above results show that with the increase in sliding speed and normal load, the Fe-base AMC changes from oxidation wear to delamination wear under cyclic stress, and then the delamination wear gradually increases.

3.4 Flash Temperature

The oxidation behavior and phase transition of the Fe-based AMCs brought on by the creation of frictional heat during dry sliding are to blame for this phenomenon. During the wear process, the temperature increases due to the frictional heat generated. This leads to the formation of an oxide layer. The frictional contact flash temperature, which represents the local temperature at the point of contact with the rough body during sliding wear, has a short duration (Ref 32). Direct measurement of temperature values is challenging due to the short time frame and small contact area involved. Therefore, theoretical estimation is often used. In this study, using the Liu model (Ref 33), it is possible to calculate the contact flash temperature between the friction pair and the Fe-based AMC:

$$T_f = \frac{1}{4} \frac{\mu v \sqrt{\pi F_N H}}{(k_1 + k_2)} \quad (\text{Eq 1})$$

where T_f is the flash temperature, μ is the COF, v is the sliding speed, F_N is the normal load, H is the nano-indentation hardness of the coating (10.04 GPa), and k_1 is the thermal conductivity of the coating (since the current work cannot obtain the thermal properties of Fe-based AMCs alone, according to the previous work of Lu et al., $k = 8.3 \text{ Wm}^{-1} \text{ }^\circ\text{C}^{-1}$ (Ref 34)), and k_2 is the thermal conductivity of the Si_3N_4 sphere ($18.0 \text{ Wm}^{-1} \text{ }^\circ\text{C}^{-1}$). Table 3 presents the computation results. For typical weights of 5N and 10N, the contact flash temperature reaches 298 and 347 $^\circ\text{C}$, respectively, at a sliding speed of 0.1 m/s. These temperatures are significantly lower than the glass transition temperature of the Fe-based AMC at 620 $^\circ\text{C}$ (Ref 26). However, the contact flash temperature quickly surpasses T_g (glass transition temperature) and T_x (phase transition temperature) when the sliding speed is greater than 0.3 m/s.

At high temperatures, it is known that Fe-based AMCs are prone to oxidation (Ref 31, 35). As presented in Table 3, during the process of dry friction and wear, the contact flash temperature between the friction pair and the Fe-based AMC increases rapidly with higher sliding speeds and normal loads, eventually approaching or surpassing the T_g and T_x points of the coating. During dry friction and wear, this high-temperature environment encourages the oxidation and crystallization of the Fe-based AMC. EDS scanning of the worn surface of the Fe-based AMC, as shown in Fig. 10, demonstrates that the degree of oxidation in the coating increases with higher sliding speeds and normal loads. Under high sliding speed conditions, oxidation takes place in the wear area. As indicated in Table 4, as the sliding velocity rises from 0.1 to 0.3 m/s at 5N, the atomic percentage of oxygen on the coated surface decreases from 47.73 to 43.68%. This can be attributed to cyclic stress acting on the coating surface, initiating crack formation as the sliding speed increases. As a result, a portion of the oxide layer

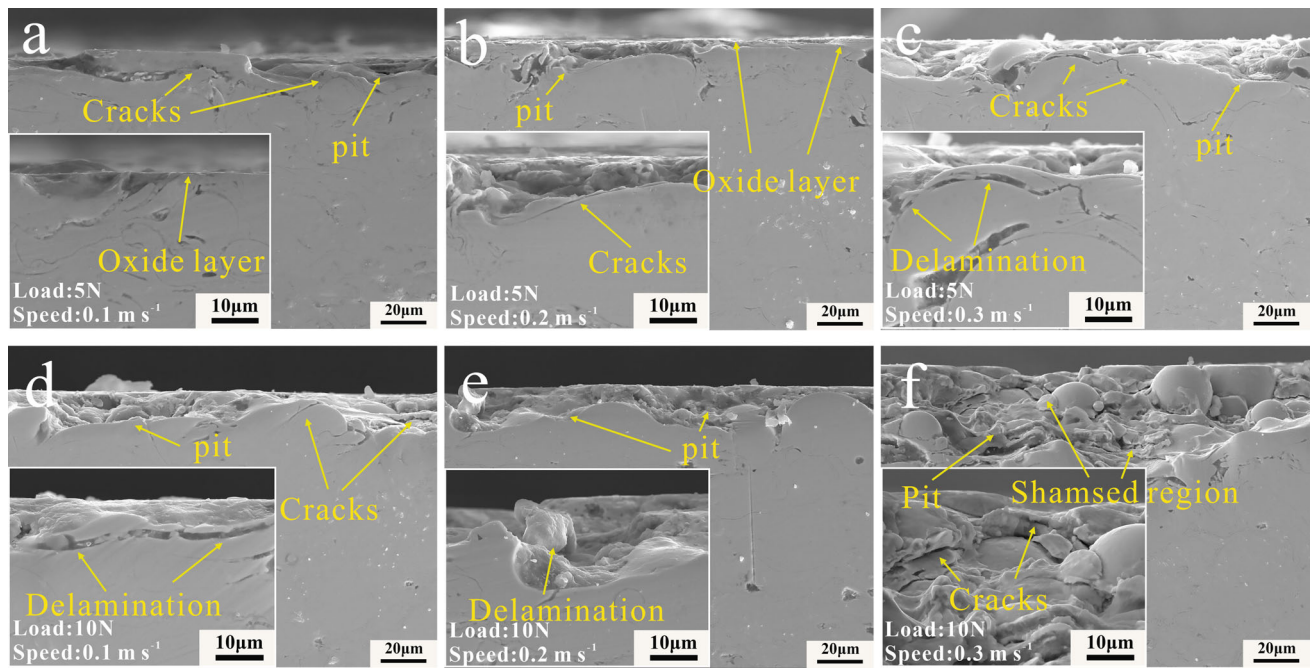


Fig. 9 SEM images of the wear surface of Fe-based AMC: (a) (b) (c) the normal load is 5N, and the sliding velocity is 0.1-0.3 m/s; (d) (e) (f) The normal load is 10N, and the sliding speed is 0.1-0.3 m/s

Table 3 Calculated values of the friction contact flash temperature of the coating under different normal loads and sliding speeds

	0.1 m/s	0.2 m/s	0.3 m/s
5N	298 °C	604 °C	974 °C
10N	347 °C	641 °C	897 °C

on the coating surface starts to bend and flake, which lowers the oxygen concentration. The oxygen concentration on the coated surface, on the other hand, rises with increasing sliding speed when the load is 10N. This may be due to the excessive flash temperature generated by the coating friction at a sliding speed of 0.3 m/s (reaching 897 °C), causing the coating grinding chips to be unable to leave the coating surface before being crushed and oxidized. This leads to an increase in the oxygen content on the coating surface. The oxidized chips also generate lubrication, which contributes to a decrease in the coefficient of friction of the coating at this stage.

Furthermore, the hardness of the worn surface at 10N and 0.1 m/s is slightly higher than that at 5N, as depicted in Fig. 11a. However, at 30 µm from the worn surface, the coating hardness remains the same. This indicates that the oxide layer gradually peels off from the coating surface, and the hardness of the coating surface is higher than that of the oxide layer. Detonation spraying, which accelerates powder particles to high speeds (1200 m/s), provides the coating with a dense structure and reasonably high surface hardness, despite there still being some uncoated patches on the coating surface. As a result, the surface of the Fe-based AMC created via detonation spraying is less likely to crack and peel, and oxidation wear is the main mode of wear at this point. Additionally, the presence of a few pits on the worn marks suggests that delamination

wear also contributes to the coating wear under the applied load and sliding speed.

Based on Table 3, amorphous crystallization behavior and the precipitation of nanoscale crystal phases result when the contact flash temperature between the coating and the friction pair is higher than the crystallization temperature of the Fe-based AMC (Ref 21, 26). This will undoubtedly increase the hardness of the coated worn surface. As shown in Fig. 11, a notable increase in surface microhardness is observed in the worn region when a normal load of 5N and a sliding speed of 0.3 m/s are applied. Although the precipitation of nanocrystals can strengthen the surface of the wear marks, the precipitation of too many brittle nanocrystals will further reduce the toughness of the wear marks, resulting in cracks more easily. As the plastic toughness of amorphous alloys heavily influences wear resistance, increased brittleness consequently decreases the wear resistance of amorphous alloys (Ref 36). As a result, when operating at high speed (0.3 m/s) and high load (10N), as opposed to low speed (0.1 m/s) and low load (5N), the Fe-based AMC experiences a higher rate of wear. Therefore, when load and sliding speed increase, the coating becomes more susceptible to delamination wear, with the wear rate of Fe-based AMCs dramatically increasing at a normal load of 10N.

Figure 12 illustrates the fitted Fe 2p, Cr 2p, and Mo 3d XPS spectra from the Fe-based AC wear surface at different normal loads (5N and 10N) of 0.3 m/s. There are three component states for Fe indicated by the Fe 2p spectra, which are Fe⁰ (707.6 eV), FeO (710.6 eV), and Fe₂O₃ (712.3 eV, 714.1 eV). Metallic Cr⁰ (574.7 eV), Cr₂O₃ (586.3 eV), and CrO₃ (578.9 eV) are three more Cr states that are present. The metallic state of Mo⁰ is indicated by the peak at 231.9 eV in the Mo 3d spectrum, followed by the peaks at 227.9 and 232.8 eV for MoO₂ and 222.3 and 235.4 eV for MoO₃. The findings of the XPS examination supported the existence of the oxide phases. The content of oxide on the surface of the coating under 10N load is slightly lower than that at 5N, but the decrease in Fe⁰,

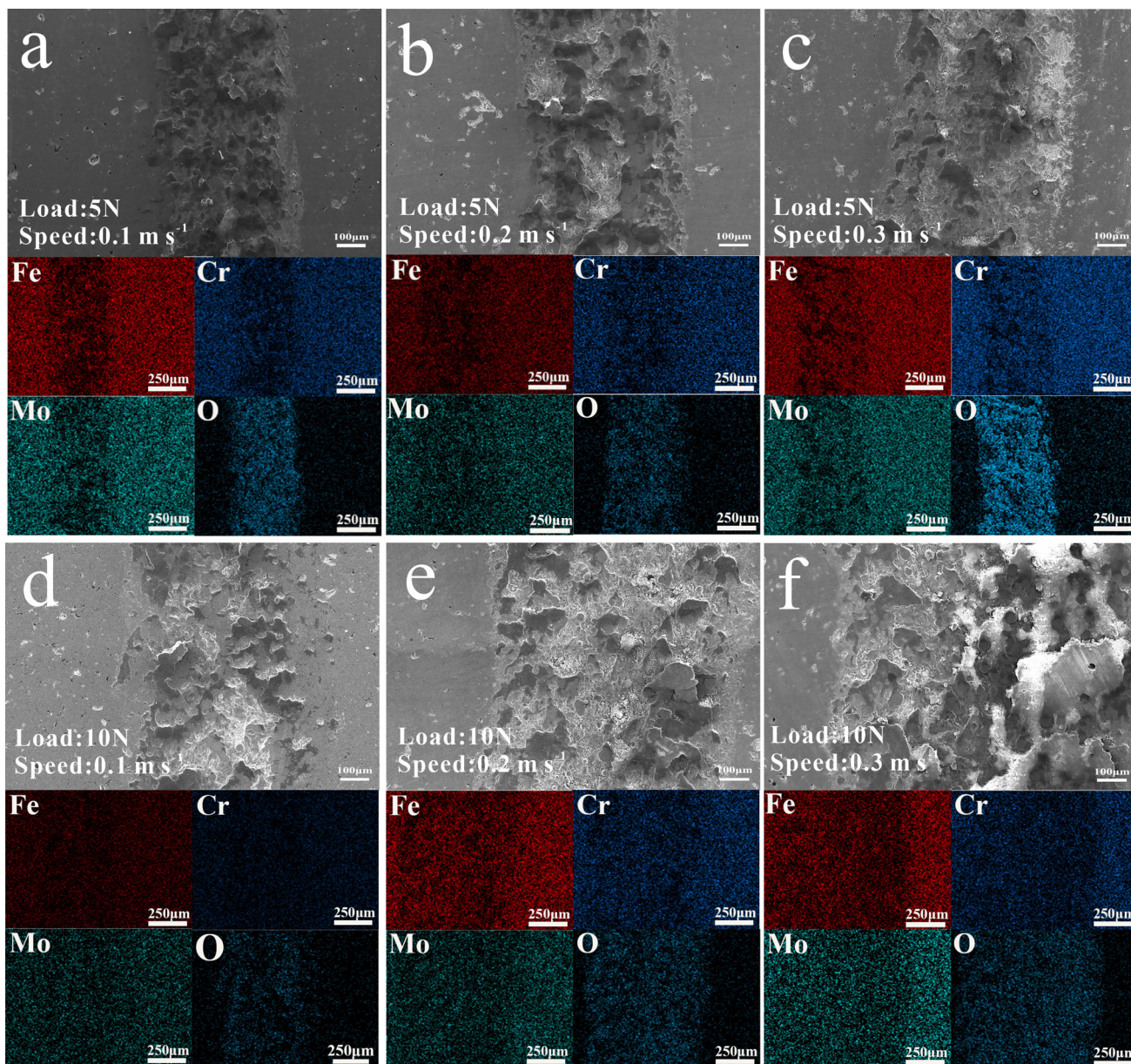


Fig. 10 Distribution of EDS scanning elements on the coating surface under different normal loads and sliding speeds

Table 4 Distribution of EDS scanning element content on the coating surface under normal load of 5N and 10N and sliding speed of 0.1 and 0.3 m/s

Element						
Atomic percent%	O	Fe	C	Cr	Si	Mo
5N-0.1 m/s	47.73	12.37	12.03	6.19	6.37	2.45
5N-0.3 m/s	43.68	15.49	7.94	7.87	6.16	3.21
10N-0.1 m/s	25.45	13.82	9.84	6.83	2.37	2.70
10N-0.3 m/s	38.5	11.74	10.15	5.84	1.81	2.28

Cr⁰ and Mo⁰ indicates that the cyclic stress increases the oxidation degree of the coating under high load, and the coating spalling leads to the decrease in the coating oxide content,

which proves once again that the increase in load can promote the spalling of the Fe-based AMC.

4. Conclusions

Detonation spraying was used to develop the Fe-based AMC on 316L stainless steel. Under normal loads of 5N and 10N and sliding velocities of 0.1 to 0.3 m/s, the dry sliding friction and wear mechanism between the Fe-based AMC and Si₃N₄ ball was investigated. The main conclusions are as follows:

- 1) The detonation-sprayed Fe-based AMC has a good amorphous structure and no obvious crystallization phenomenon. The Fe-based AMC offers desirable material properties, such as sufficient thickness ($174 \pm 10 \mu\text{m}$),

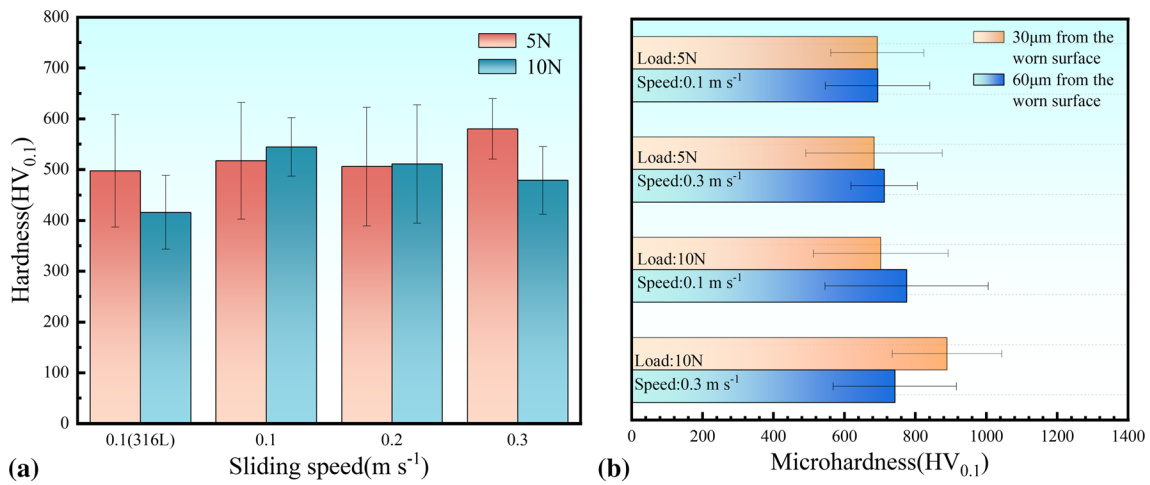


Fig. 11 Hardness of the wear surface of the coating under different normal loads and sliding speeds (a) Hardness of coating cross section at 30 and 60 distances from the wear surface at normal loads of 5N and 10N (b) sliding speeds of 0.1 and 0.3 m/s

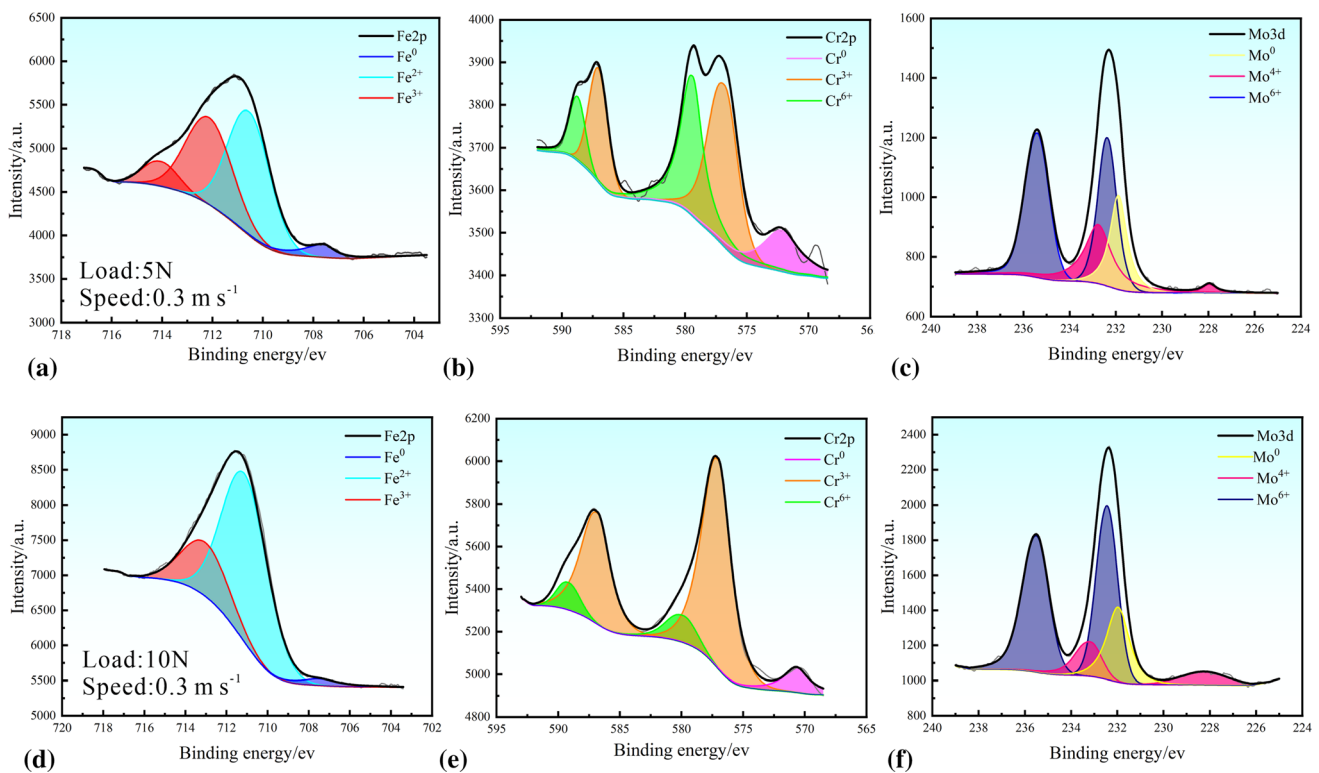


Fig. 12 Fe 2p, Cr 2p, and Mo 3d spectra fitted on the coated wear surface: (a) (b) (c) the normal load is 5N and the sliding speed is 0.3m/s (d) (e) (f) The normal load is 10N and the sliding speed is 0.3m/s

low porosity (less than 1.2 vol.%), and high hardness ($783 \pm 8 \text{ Hv}_{0.1}$), making it a suitable choice for various applications requiring enhanced surface protection and durability.

2) Under dry sliding wear conditions, the wear rate of the Fe-based AMC ranges from $(0.16\text{--}2.53) \times 10^{-6} \text{ mm}^3 \text{ N}^{-1} \text{ m}^{-1}$, which is up to 5 times less than that of 316L stainless steel substrate. It appears that the applied normal load has a more pronounced effect on the wear rate compared to the sliding velocity. This implies that the wear resistance of the coating is more influenced by the force applied perpendicular to the surface

rather than the speed at which the sliding occurs. These results highlight the superior wear resistance of the Fe-based AMC.

- 3) The wear mechanism of the Fe-based AMC changes from oxidation wear to delamination wear with a little presence of abrasive wear as the usual load and sliding speed rise. At low loads and sliding speeds, due to the influence of the contact flash temperature, the precipitated nanocrystalline in the coating increases its hardness; therefore, the coating is mainly dominated by oxidation wear.
- 4) The higher normal load and sliding speed increase the precipitation of nanocrystals and oxidation behavior in

the coating under the high shear stress and contact flash temperature, this can increase the coating's brittleness, coupled with the rapid breakage of the oxide layer, resulting in increased brittleness of the coating, and significantly increase the wear rate of the coating. Consequently, the wear mechanism shifts toward delamination wear.

Acknowledgments

This work was supported by the National Natural Science Foundation of China (No. 52075234), and the Natural Science Foundation of Gansu Province (23JRRA802).

Author contributions

CL contributed to conceptualization, funding acquisition, resources, supervision, and writing—review & editing. RW contributed to conceptualization, methodology, software, investigation, data curation, formal analysis, and writing—original draft. XX contributed to software and investigation. SL contributed to visualization and formal analysis. HZ contributed to conceptualization, funding acquisition, resources, supervision, and writing—review & editing. WL contributed to resources and supervision.

Competing interest

The authors declare that they have no known competing financial interests or personal relationships that could have appeared to influence the results and opinions stated in this paper.

References

1. Q.Y. Wang, X.Z. Wang, H. Luo, and J.L. Luo, A Study on Corrosion Behaviors of Ni-Cr-Mo Laser Coating, 316 Stainless Steel and X70 Steel in Simulated Solutions with H₂S and CO₂, *J. Surf. Coat. Technol.*, 2016, **29**(1), p 250–257
2. O. Ertugrul, T.M. Enrici, H. Paydas, E. Saggionetto, F. Boschini, and A. Mertens, Laser Cladding of TiC Reinforced 316L Stainless Steel Composites: Feedstock Powder Preparation and Microstructural Evaluation, *J. Powder Technol.*, 2020, **37**(5), p 384–396
3. N. Jeyaprakash, C.H. Yang, and S. Sivasankaran, Laser Cladding Process of Cobalt and Nickel Based Hard-Micron-Layers on 316L-Stainless-Steel-Substrate, *J. Mater. Manuf. Process.*, 2020, **35**(2), p 142–151
4. T. Maurizi Enrici, O. Dedry, F. Boschini, J.T. Tchuidjang, and A. Mertens, Microstructural and Thermal Characterization of 316L+WC Composite Coatings Obtained by Laser Cladding, *J. Adv. Eng. Mater.*, 2020, **22**(12), p 2000291
5. B. Aktas, M. Toprak, A. Calik, and A. Tekguler, Effect of Pack-Boriding on the Tribological Behavior of Hardox 450 and HiTuf Steels, *J. Rev. Adv. Mater. Sci.*, 2020, **59**(1), p 314–321
6. C. Carboga, B. Aktas, and B. Kurt, Dry Sliding Wear Behavior of Boron-Doped 205 Manganese Steels, *J. Mater. Eng. Perform.*, 2020, **29**(5), p 3120–3126
7. B. Aktas, V. Balak, and C. Carboga, Dry Sliding Wear Behavior of Boron-Doped AISI 1020 Steels, *J. Acta Physica Polonica A*, 2017, **132**(3), p 455–457
8. S.L. Wang and S. Yi, The Corrosion Behaviors of Fe-Based Bulk Metallic Glasses in a Sulfuric Solution at 70 Degrees C, *J. Intermet.*, 2010, **18**(10), p 1950–1953
9. H. Zhai, H. Wang, and F. Liu, A Strategy for Designing Bulk Metallic Glass Composites with Excellent Work-Hardening and Large Tensile Ductility, *J. Alloys Compd.*, 2016, **685**, p 322–330
10. Q. Yan, Y. Gao, C. Du, Z. Yao, and Y. Mo, Ultrasonic-Assisted Shearing Characteristics of Fe-Based Amorphous Alloy Strips, *J. Mater. Eng. Perform.*, 2022, **31**(12), p 9630–9642
11. P. Rezaei-Shahreza, A. Seifoddini, and S. Hasani, Thermal Stability and Crystallization Process in a Fe-Based Bulk Amorphous Alloy: The Kinetic Analysis, *J. Non-Cryst. Solids*, 2017, **471**, p 286–294
12. C. Zhang, Z. Chu, F. Wei, W. Qin, Y. Yang, Y. Dong, and L. Wang, Optimizing Process and the Properties of the Sprayed Fe-Based Metallic Glassy Coating by Plasma Spraying, *J. Surf. Coat. Technol.*, 2017, **319**, p 1–5
13. J. Su, J.J. Kang, W. Yue, G.Z. Ma, Z.Q. Fu, L.N. Zhu, and C.B. Wang, Comparison of Tribological Behavior of Fe-Based Metallic Glass Coatings Fabricated by Cold Spraying and High Velocity Air Fuel Spraying, *J. Non-Cryst. Solids*, 2019, **522**, p 119582
14. J.J. Xu, J.J. Kang, W. Yue, Z.Q. Fu, L.N. Zhu, and D.S. She, High-Temperature Tribological Property of Fe-Based Amorphous Alloy Coating, *J. Non-Cryst. Solids*, 2021, **573**, p 121136
15. K. Chokethawai, D.G. McCartney, and P.H. Shipway, Microstructure Evolution and Thermal Stability of an Fe-Based Amorphous Alloy Powder and Thermally Sprayed Coatings, *J. Alloys Compd.*, 2009, **480**(2), p 351–359
16. H.C. Fals, M.S. Orozco, L.A. Lourencato, and C.R. Camello Lima, Abrasive Wear Behavior of Fe-Based Amorphous/Nanocrystalline Coatings Deposited by High-Velocity Oxygen Fuel and Wire Arc Spray, *J. Mater. Eng. Perform.*, 2023, **32**(5), p 2455–2462
17. H. Guo, S. Zhang, W. Sun, and J. Wang, Differences in Dry Sliding Wear Behavior Between HVOF-Sprayed Amorphous Steel and Crystalline Stainless Steel Coatings, *J. Mater. Sci. Technol.*, 2019, **35**(5), p 865–874
18. E. Sadeghi and S. Joshi, Chlorine-induced high-temperature corrosion and erosion-corrosion of HVOF and HVOF-sprayed amorphous Fe-based coatings, *J. Surf. Coat. Technol.*, 2019, **371**, p 20–35
19. H. Kasturi, T. Paul, S. Biswas, S.H. Alavi, and S.P. Harimkar, Sliding Wear Behavior of Spark-Plasma-Sintered Fe-Based Amorphous Alloy Coatings on Cu-Ni Alloy, *J. Mater. Eng. Perform.*, 2018, **27**(7), p 3629–3635
20. Z. Chu, F. Wei, X. Zheng, C. Zhang, and Y. Yang, Microstructure and Properties of TiN/Fe-Based Amorphous Composite Coatings Fabricated by Reactive Plasma Spraying, *J. Alloys Compd.*, 2019, **785**, p 206–213
21. S. Cui, H. Zhai, W. Li, X. Fan, X. Li, W. Ning, and D. Xiong, Microstructure and Tribological Properties of Fe-Based Amorphous Coating Prepared by Detonation Spray, *J. Non-Cryst. Solids*, 2021, **556**, p 120564
22. H. Yuan, H. Zhai, W. Li, D. He, B. Cheng, and L. Feng, Study of Dry Sliding Wear Behavior of a Fe-Based Amorphous Coating Synthesized by Detonation Spraying on an AZ31B Magnesium Alloy, *J. Mater. Eng. Perform.*, 2021, **30**(2), p 905–917
23. G.Y. Koga, R. Schulz, S. Savoie, A.R.C. Nascimento, Y. Drolet, C. Bolfarini, and W.J. Botta, Microstructure and Wear Behavior of Fe-Based Amorphous HVOF Coatings Produced from Commercial Precursors, *J. Surf. Coat. Technol.*, 2017, **309**, p 938–944
24. S. Mahade, S.A. Awe, S. Bjorklund, F. Lukac, R. Musalek, and S. Joshi, Sliding Wear Behavior of a Sustainable Fe-Based Coating and its Damage Mechanisms, *J. Wear*, 2022, **500**, p 204375
25. H. Zhang, Y. Xie, L. Huang, S. Huang, X. Zheng, and G. Chen, Effect of Feedstock Particle Sizes on Wear Resistance of Plasma Sprayed Fe-Based Amorphous Coatings, *J. Surface Coat. Technol.*, 2014, **258**, p 495–502
26. X. Li, H. Zhai, W. Li, S. Cui, W. Ning, and X. Qiu, Dry Sliding Wear Behaviors of Fe-Based Amorphous Metallic Coating Synthesized by D-Gun Spray, *J. Non-Cryst. Solids*, 2020, **537**, p 120018
27. D.J. Whitehouse, The Properties of Random Surfaces of Significance in Their contact. 1971
28. J.B. Cheng, X.B. Liang, Z.H. Wang, and B.S. Xu, Dry Sliding Friction and Wear Properties of Metallic Glass Coating and Martensite Stainless Coating, *J. Tribol. Int.*, 2013, **60**, p 140–146
29. Q.B. Zhang and J. Zhao, A Review of Dynamic Experimental Techniques and Mechanical Behaviour of Rock Materials, *J. Rock Mech. Rock Eng.*, 2014, **47**(4), p 1411–1478

30. B.T. Jang, S.S. Kim, and S. Yi, Wear Behaviors of a Fe-Based Amorphous Alloy in Ambient Atmosphere and in Distilled Water, *J. Met. Mater. Int.*, 2014, **20**(1), p 55–61
31. H.H. Hsieh, W. Kai, R.T. Huang, D.C. Qiao, and P.K. Liaw, Air Oxidation of an Fe₄₈Cr₁₅C₁₅Mo₁₄B₆Er₂ Bulk Metallic Glass At 600–725 °C, *J. Mater. Trans.*, 2007, **48**(7), p 1864–1869
32. P.H. Thomas, The Surface Temperature of Rubbing Solids, *J. Proc. R. Soc. A*, 1950, **223**, p 29–40
33. Y. Liu, A. Erdemir, and E.I. Meletis, A Study of the Wear Mechanism of Diamond-Like Carbon Films, *J. Surf. Coat. Technol.*, 1996, **82**, p 48–56
34. D.J. Whitehouse and J.F. Archard, The Properties of Random Surfaces of Significance in Their Contact, *J. Proc. R. Soc. London*, 1971, **316**(1524), p 97–121
35. B. Zhang, J. Chen, and X. Liang, Effects of Cr and Mo Additions on Formation and Mechanical Properties of Arc-Sprayed FeBSiNb-Based Glassy Coatings, *J. Non-Cryst. Solids*, 2018, **499**, p 245–251
36. Z. Liao, N. Hua, W. Chen, Y. Huang, and T. Zhang, Correlations Between the Wear Resistance and Properties of Bulk Metallic Glasses, *J. Intermet.*, 2018, **93**, p 290–298

Publisher's Note Springer Nature remains neutral with regard to jurisdictional claims in published maps and institutional affiliations.

Springer Nature or its licensor (e.g. a society or other partner) holds exclusive rights to this article under a publishing agreement with the author(s) or other rightsholder(s); author self-archiving of the accepted manuscript version of this article is solely governed by the terms of such publishing agreement and applicable law.